

Magnetic and electronic crossovers in graphene nanoflakesShreemoyee Ganguly,¹ Mukul Kabir,^{2,3} and Tanusri Saha-Dasgupta⁴¹*Thematic Unit of Excellence on Computational Materials Science, S. N. Bose National Centre for Basic Sciences, Kolkata 700098, India*²*Department of Physics, Indian Institute of Science Education and Research, Pune 411008, India*³*Centre for Energy Science, Indian Institute of Science Education and Research, Pune 411008, India*⁴*Department of Condensed Matter Physics and Materials Science, S. N. Bose National Centre for Basic Sciences, Kolkata 700098, India*

(Received 21 December 2016; published 12 May 2017)

Manipulation of magnetic and electronic structures of graphene nanoflakes is of great technological importance. Here, we systematically study the magnetic and electronic phases of graphene nanoflakes within first-principles calculations. We illustrate the intricate shape and size dependence on the magnetic and electronic properties and further investigate the effects of carrier doping, which could be tuned by gate voltage. A crossover from the nonmagnetic to magnetic phase is observed at a critical flake size for the flakes without sublattice imbalance. We identify this as originating from the armchair defects at the junctions of two sublattices on the edge. Electron or hole doping simultaneously influences the magnetic and electronic structures and triggers phase crossover. Beyond a critical doping, antiferromagnetic to ferromagnetic phase crossover is observed for the flakes without sublattice imbalance. In contrast, suppression of magnetism and a possible crossover from the magnetic to nonmagnetic phase is observed for flakes with sublattice imbalance. Simultaneous with magnetic phase changes, a semiconductor to (half) metal transition is observed upon carrier doping. Our findings should have important implications in graphene-based spintronics.

DOI: [10.1103/PhysRevB.95.174419](https://doi.org/10.1103/PhysRevB.95.174419)**I. INTRODUCTION**

Plausible applications in spin-based electronics and information processing [1–5] have made unconventional magnetism in an sp^2 -bonded two-dimensional (2D) hexagonal network of C atoms in graphene a topic of recent discussion. Carbon-based materials have unique advantages in this regard due to very weak spin-orbit and hyperfine coupling [6–8] and high spin-wave stiffness [9]. Thus, magnetic carbon structures are expected to exhibit higher Curie temperature and spin correlation length compared to conventional magnets [10]. Further, the spin transport in graphene could be manipulated easily by external perturbations such as electric fields [11].

Magnetism in otherwise nonmagnetic graphene can be induced by the presence of point/extended defects [12–16] or through adatom adsorption [17,18]. Alternatively, the nontrivial π -electron-driven magnetism can be induced at the edges in a finite graphene nanoflake (GNF) due to the localized edge states [19–23]. While the π electron of C atoms on zigzag edges has localized character, no such localization is expected for the armchair edge type. Although graphene nanostructures have been fabricated with success [24–26], precise control over the edge type has been limited until recently. Using a nanofabrication technique and scanning tunneling microscopy, nanoribbons with precise zigzag edges have been fabricated, and a robust long-range magnetic order has been observed at room temperature [27]. Further, a semiconductor to metal transition accompanied by switching in the magnetic ordering between the edges has been predicted as a function of ribbon width [27].

Graphene is a bipartite hexagonal lattice formed by two interpenetrating triangular sublattices A and B. According to the predictions of single-band Hubbard model, spins localized at the zigzag edge align in parallel if they belong to the same sublattice and become antiparallel if they belong to different sublattices [28]. Thus, the total spin of the ground

state follows Lieb's theorem, $2S = N_A - N_B$, with N_A and N_B being the number of C atoms belonging to the A and B sublattices, respectively [29]. This picture has been confirmed through density-functional-theory-based calculations in passivated flakes [28,30]. Further, a magnetic phase change has been predicted in hexagonal flakes due to carrier doping [30]. As the intrinsic magnetic ordering and corresponding ground-state magnetization are related to the sublattice identity of the edge atoms and total sublattice imbalance, a unified picture of the size and shape dependence of magnetism in nanoflakes is necessary, which has not yet been fully explored.

Here, we systematically address this issue within first-principles calculations by considering graphene nanoflakes with varied shapes and sizes. Nanoflakes with arbitrary shapes can be classified by sublattice imbalance; for flakes with sublattice imbalance $N_A \neq N_B$, and for those without imbalance $N_A = N_B$. We consider flakes with rhombohedral (R), hexagonal (H), triangular (T), and pentagonal (P) shapes. While R and H flakes have $N_A = N_B$, T and P flakes have $N_A \neq N_B$. In order to investigate only the π electrons, the in-plane dangling bonds are passivated with a single hydrogen atom. For the nanoflakes without any sublattice imbalance, the prediction of Lieb's theorem, $S = 0$, may be satisfied either with a nonmagnetic solution or with a fully compensated intrinsic magnetic ordering. This may lead to a quantum phase transition with flake size [28]. Indeed, for both R and H shapes, we find that carbon atoms at the edge develop local moments beyond a critical size, and a crossover from the nonmagnetic to compensated ferrimagnetic phase takes place. We characterize this critical size with the armchair defect density at the edge, which is defined as the ratio of the number of armchair bonds at the junction of the A and B sublattices and the number of zigzag bonds. In contrast, the flakes with sublattice imbalance, T and P flakes, are always found to be magnetic, independent of their sizes.

Further, manipulation of the intrinsic magnetic and corresponding electronic properties by external perturbations is key to spintronics applications. Thus, in addition to undoped flakes, we investigate the carrier-doped flakes. Doping could be experimentally achieved with applied gate voltage. In this context, the single-hole doping in the half-filled Hubbard model in the Nagaoka limit [31] of an infinite bipartite lattice with essentially infinite Coulomb interaction predicts a magnetic phase transition. In the present cases of nanoflakes, neither of the Nagaoka limits are satisfied. Nonetheless, we observe a change in the magnetic structure upon carrier doping, and a shape-dependent complex evolution of magnetic phase is predicted. Together with the changes in magnetic phases, a semiconductor to (half) metal transition is observed. With the current state of advancement in controlled experimental techniques, we hope that our theoretical predictions will stimulate further experimental activity.

II. COMPUTATIONAL DETAILS

Calculations were carried out within density-functional theory (DFT) in the plane-wave basis, as implemented in the Vienna Ab initio Simulation Package (VASP) [32,33]. The projector augmented-wave pseudopotential was used with a plane-wave cutoff of 800 eV [34]. For the exchange-correlation functional, we used the Perdew-Burke-Ernzerhof (PBE) form of the generalized gradient approximation (GGA) [35]. The reciprocal space integrations were carried out at the Γ point. Within the periodic setup of the calculations, flakes were placed in simple cubic supercells such that the periodic images were separated by at least 12 Å of vacuum space, which makes the interaction between the images negligible. Nanoflakes were optimized until the forces on each atom were less than 5×10^{-3} eV/Å. Further, to understand the effect of electron-electron correlation beyond GGA, some of the calculations were repeated considering a Hubbard-like on-site Coulomb interaction, DFT + U , within the rotationally invariant approach [36].

The atom-projected local magnetic moment μ_{loc} is calculated by integrating the difference between the spin-up $[\rho_{\uparrow}(\mathbf{r})]$ and spin-down $[\rho_{\downarrow}(\mathbf{r})]$ charge densities over a Wigner-Seitz (WS) sphere centered around a specific atom, defined as $\mu_{\text{loc}} = \int_{R_{\text{WS}}} [\rho_{\uparrow}(\mathbf{r}) - \rho_{\downarrow}(\mathbf{r})] d\mathbf{r}$. Similarly, the total moment μ_{tot} of the nanoflake is calculated by integrating the difference between the spin-up and spin-down charge densities over the entire cell.

Within the present supercell approach, for the charged flakes, the Coulomb divergence is circumvented by a uniform and neutralizing jellium background [37]. Although such a strategy has limitations [38], it works quite well for homogeneous systems [39,40]. As the leading-order correction depends on the size of the supercell, some of the calculations have been repeated by doubling the supercell size. However, we did not find any significant difference between the magnetic structures given by the two sets of calculations.

We considered regular T and H flakes with sizes $m = 3, 5, 6, 8$ and $m = 3, 6, 7, 8, 9, 10$, respectively, where m is the number of hexagonal rings along their regular edge [Figs. 1(a) and 1(b)]. The sizes of the R and P flakes are denoted by $m \times n$ and $m \otimes n$, respectively, where m and n

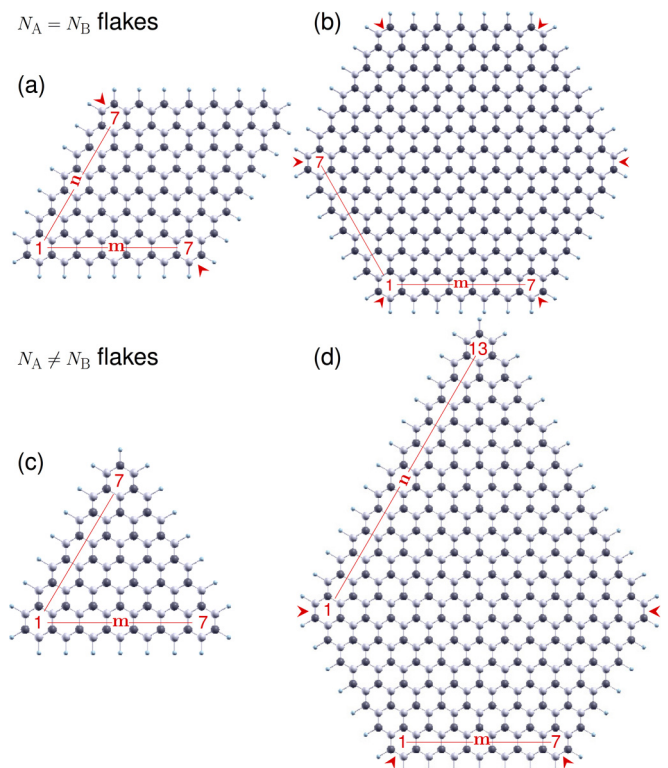


FIG. 1. Hydrogenated graphene nanoflakes, considered in the present study: (a) rhombohedral (R), (b) hexagonal (H), (c) triangular (T), and (d) pentagonal (P) flakes. Carbon atoms belonging to two sublattices are marked with black and white balls. The H atoms are shown with small blue balls. The size of the flakes is characterized by the number of hexagonal rings along the edge. While sizes of regular T and H flakes are represented by edge lengths m , the R and P flakes are represented as $m \times n$ and $m \otimes n$, respectively. The armchair defects at the junctions of the A and B sublattices are highlighted by arrowheads. The number of such defects is 2 for R flakes, 6 for H flakes, 4 for P flakes, and 0 for T flakes.

are lengths of dissimilar edges [Figs. 1(c) and 1(d)]. Flakes with sizes $3 \times 3, 3 \times 5, 3 \times 7, 4 \times 4, 5 \times 5$, and 7×7 were considered for the R flake, and flakes with sizes $4 \otimes 7, 5 \otimes 9, 7 \otimes 13$, and $8 \otimes 15$ were considered for the P flake.

III. RESULTS AND DISCUSSION

We start our discussion with undoped GNFs to illustrate the intricate shape and size dependence of the intrinsic edge magnetism. We also investigate the effect of strong electron correlation on the magnetism. With the understanding of the intricate size-, shape-, and correlation-dependent magnetism in undoped GNFs, we proceed to discuss the effect of carrier doping on the magnetic and electronic structures.

A. Shape and size dependence of edge magnetism

We find that the intrinsic magnetic structures of the GNFs are strongly dependent on both nanoflake shape and their size. The magnetic behavior of undoped flakes of four different shapes, H, R, T, and P, is summarized in Fig. 2.

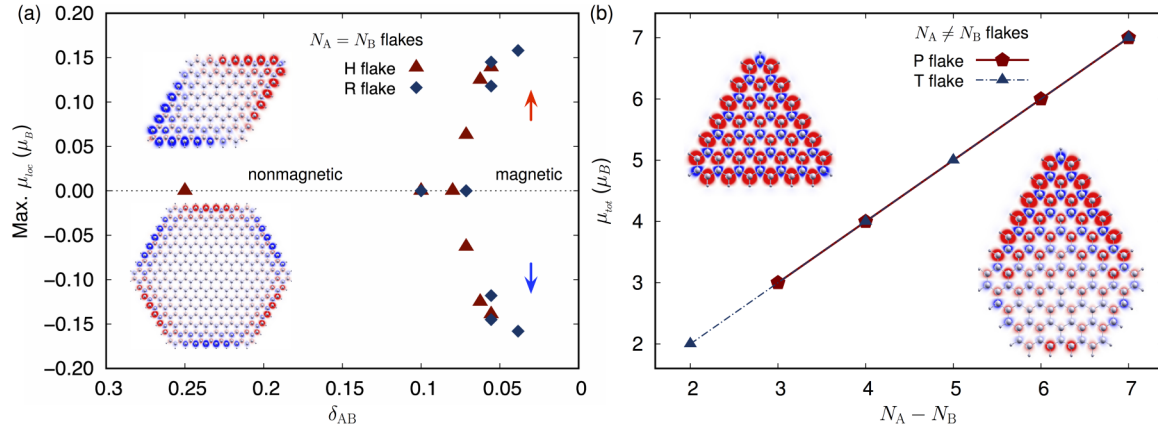


FIG. 2. Size- and shape-dependent magnetism in graphene nanoflakes. The magnetic behavior of H and R flakes is summarized in (a), while that of P and T flakes is summarized in (b). For $N_A = N_B$ flakes (H or R flakes), a nonmagnetic (zero value of μ_{loc}) to compensated ferrimagnetic transition (nonzero value of μ_{loc}) is observed for the critical value of the armchair defect concentration at the edge. The latter is given by $\delta_{AB} = N_{arm}/N_{tot}$, with N_{arm} and N_{tot} being the number of armchair defects and total number of zigzag bonds along the edge, respectively. In contrast, the $N_A \neq N_B$ flakes (P or T flakes) are always magnetic, and the plot of the total moment of the flakes μ_{tot} with the sublattice imbalance $N_A - N_B$ shows a linear behavior. Representative ground-state magnetization densities, with up (down) spin densities marked in red (blue), for the magnetic R and H flakes are shown in the top and bottom insets in (a), respectively, while those for T and P flakes are shown in the top and bottom insets of (b), respectively.

The scenario for the flakes without any sublattice imbalance, i.e., R and H flakes, is particularly nontrivial, and a size-dependent quantum phase transition is observed in the nonmagnetic to compensated ferrimagnetic transition. The compensated ferrimagnetic state is characterized by zero total moment but nonzero local moment. Plotting the maximum value of the local moment of the edge C atoms as a function of size [Fig. 2(a)], we find that only beyond a critical size do the carbon atoms at the edge develop a local moment. As seen from the plots of magnetization density, shown in the insets of Fig. 2(a), for the magnetic R and H flakes, edge moments belonging to any particular sublattice (A or B) are ferromagnetically coupled among themselves (the magnetization being either all pointed up or all pointed down), while the edge moments belonging to different sublattices are coupled antiferromagnetically (the magnetizations being directed oppositely), thereby giving rise to a compensated ferrimagnetic state. This picture is consistent with the predictions from the Hubbard model and agrees well with the previous DFT calculations for H flakes [28,30]. However, the origin of this size dependence has not been addressed previously. To characterize the observed magnetic phase transition with flake size, we define a unitless quantity δ_{AB} , which relates to the armchair defects along the entire edge of the flake. There exists an armchair bond at the junctions of the A and B sublattices (Fig. 1), where electrons are delocalized, that is thus detrimental for magnetism. Therefore, in the context of magnetism on a zigzag edge, such armchair bonds act as defects. We define the defect density as $\delta_{AB} = N_{arm}/N_{tot}$, where N_{arm} (N_{tot}) is the number of armchair defects (total number of zigzag bonds) along the edge. Thus, δ_{AB} decreases with increasing flake size. We find that beyond a critical flake size with corresponding $\delta_{AB} < 0.07$, the edge atoms develop a moment, and the flakes become compensated ferrimagnetic [Fig. 2(a)]. Note the quantum phase transitions for both R and H flakes occur at similar δ_{AB} values. Although the

local moment distributions [see the insets in Fig. 2(a)] in these two types of flakes apparently look different, a closer look reveals their microscopic similarity. First, for both types of flakes, the magnetic interaction between intrasublattice edge moments is ferromagnetic, while it is antiferromagnetic between intersublattice edge moments, as discussed earlier. In both cases, the armchair defect separates two sublattice at the edge [Figs. 1(a), 1(b), and 2(a)]. Second, at the edge, the local moment distribution as a function of distance from the armchair defect behaves in a qualitatively similar fashion. For both flakes, the local moment at the edge increases with increasing distance from the armchair defect and becomes maximum for the farthest edge atom from the defect. These microscopic similarities in turn drive the quantum phase transitions for these two types of flakes at similar δ_{AB} . It is important to note that with increasing flake size ($\delta_{AB} < 0.07$) the maximum local moment at the edge μ_{loc} increases but keeps the net moment fixed at zero and thus obeys Lieb's theorem. It should be noted here that in the absence of any armchair defect ($\delta_{AB} = 0$), the flake may be viewed as an infinite zigzag nanoribbon, and the edge moment will approach that of the intrinsic graphene zigzag edge [10,20,41]. Further, it has been reported that vacancies and nonmagnetic substitutional impurities such as boron at the zigzag nanoribbon edge have a detrimental effect on the edge magnetism, and the nanoribbons become nonmagnetic beyond critical vacancy/impurity concentrations [41]. Similar behavior is anticipated for the graphene nanoflakes.

In comparison, the size-dependent magnetism in T and P flakes with sublattice imbalance is less complex. Independent of size, such $N_A \neq N_B$ flakes are found to be magnetic with the total ground-state magnetization given by $\mu_{tot} = 2S = N_A - N_B$, following Lieb's theorem [Fig. 2(b)]. Thus, with an increase in size, the sublattice imbalance increases, leading to a linear increase in μ_{tot} . For T flakes, all the edge atoms belong to a particular sublattice [Fig. 1(c)], and thus, the

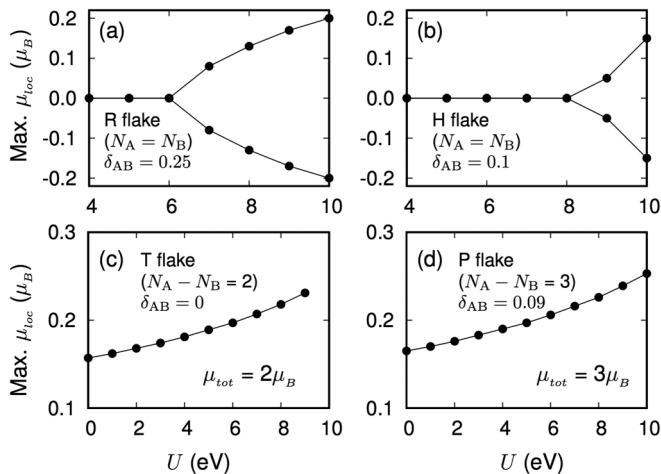


FIG. 3. Effect of on-site Coulomb interaction U on the edge magnetism. The maximum μ_{loc} calculated within DFT + U formalism are shown with varied U for (a) a 3×3 R flake, (b) an $m = 3$ H flake, (c) an $m = 3$ T flake, and (d) a $4 \otimes 7$ P flake. At a critical U , the R and H flakes become magnetic, and μ_{loc} increases further with U . In contrast, T and P flakes are always magnetic, and the calculated μ_{loc} increases with increasing U . Total moment, however, remains invariant, as an increase in local moments of atoms belonging to the A sublattice is compensated by the negative increase in local moments of atoms belonging to the B sublattice. The armchair defect density δ_{AB} (as defined in the caption of Fig. 2) for the various flakes has been quoted for reference.

interedge coupling is ferromagnetic [Fig. 2(b)]. The P flakes, on the other hand, can be viewed as a fusion of T and H structures. While the edge atoms in the triangular region belong to the same sublattice, the rest of the edges alternate between two sublattices [Fig. 1(d)]. The corresponding magnetic structure is thus commensurate with the ferromagnetic and antiferromagnetic interedge coupling between the same and different sublattices [insets in Fig. 2(b)].

Next, we study the effect of strong electron-electron correlation on the edge magnetism, which has been argued for graphene nanostructures [42–45]. For 2D graphene, local Coulomb interaction is proposed to be as large as ~ 9 eV, which is in between the values that predict a spin-liquid phase [43] and a compensated antiferromagnetic phase [44,45]. Keeping this in mind, we have repeated our calculation by supplementing the conventional PBE exchange correlation with a Hubbard-like on-site Coulomb interaction U (0–10 eV). Only one representative size has been considered for each shape (Fig. 3).

The flakes without any lattice imbalance in the size range $\delta_{AB} > 0.07$ are nonmagnetic for $U = 0$. With the increase in on-site Coulomb interaction beyond a critical value U_c , the flakes become magnetic, with the edge atoms developing a local moment [Figs. 3(a) and 3(b)]. For $U \geq U_c$, μ_{loc} increases with U , although the complete magnetic structure remains a fully compensated ferrimagnet. This scenario is similar to the nonmagnetic to magnetic phase transition obtained upon increasing flake size, which was discussed in the previous section. Thus, we conclude that both an increase in size and electron-electron correlation help in enhancing the localized

character of the edge states, thereby stabilizing magnetism. In contrast, in the presence of a lattice imbalance, the flakes are always magnetic, and the increase in U monotonically increases the local moment at the edge. However, the ground-state magnetization is maintained at $\mu_{tot} = N_A - N_B$ by a compensated increase in the A and B sublattice moments. This in turn confirms the validity of Lieb’s theorem irrespective of the level of theoretical approximation toward electron correlation. Due to the absence of an accurate estimate of U for finite-size nanoflakes and due to the fact that the flake size and U affect the intrinsic magnetic structure in a similar fashion, we ignore explicit incorporation of Coulomb interaction for the rest of the paper. Rather, we will consider the larger flakes with $\delta_{AB} < 0.07$, which are magnetic even in the absence on-site Coulomb interaction.

B. Effects of carrier doping on edge magnetism

Next, we investigate the effect of carrier doping on the edge magnetism for nanoflakes with different shapes. We consider both electron and hole doping with concentrations ρ_c in the range 10^{13} – 10^{14} cm^{-2} . Such a high ρ_c has been experimentally achieved [15,46,47]. Like for the undoped flakes, the effect of carrier doping is found to be strongly shape dependent with a sharp distinction between flakes with and without sublattice imbalance. Concomitant with magnetic phase crossover, an electronic phase change is also observed due to carrier doping, which is fundamentally interesting and could be of technological importance.

We first discuss the undoped flakes with $N_A \neq N_B$, which, independent of size, is magnetic [Fig. 2(b)]. As discussed, the interedge coupling in T flakes is ferromagnetic with ground-state magnetization $\mu_{tot} = N_A - N_B$. Thus, the undoped T flakes with $m = 3$ and 8 have net magnetic moments of $2\mu_B$ and $7\mu_B$, respectively [Fig. 4(a)]. Electron (hole) doping in these flakes decreases the value of μ_{tot} to $N_A - N_B - n^{e(h)}$, where $n^{e(h)}$ is the number of doped electrons (holes). Thus, μ_{tot} monotonically decreases with increasing carrier doping [Fig. 4(a)], and the $m = 3$ flake becomes nonmagnetic beyond doping of one hole or one electron. For the larger $m = 8$ T flake, μ_{tot} decreases to $4\mu_B$ due to three-electron (-hole) doping, which corresponds to a carrier doping of 1.79×10^{14} cm^{-2} . The P-flake magnetism with carrier doping is found to be qualitatively similar to that of the T flakes.

To understand the microscopic origin of such behavior in the flakes, we calculated μ_{loc} for the edge atoms [Fig. 4(b)] and investigated the partial charge density of the doped electron (hole), shown for the $m = 8$ T flake and $4 \otimes 7$ P flakes [Figs. 5(a)–5(d)]. For both flakes, we find that the doped electron is distributed mainly on the edge atoms and distributed entirely on a particular (say, A) sublattice [Figs. 5(a)–5(c)]. Further, the doped electrons occupy the minority p_z channel, which leads to a decrease in calculated μ_{tot} with carrier doping [Fig. 4(b)]. Concurrently, μ_{tot} decreases by $n^{e(h)}\mu_B$ from the neutral ground state. However, for P flakes, such a picture breaks down at higher doping concentrations, and the corresponding ground-state magnetic moment is found to be higher than expected, $N_A - N_B - n^{e(h)}$. At the higher doping limit beyond 9.62×10^{13} cm^{-2} , although the carrier is predominantly distributed over the A sublattice, a fraction

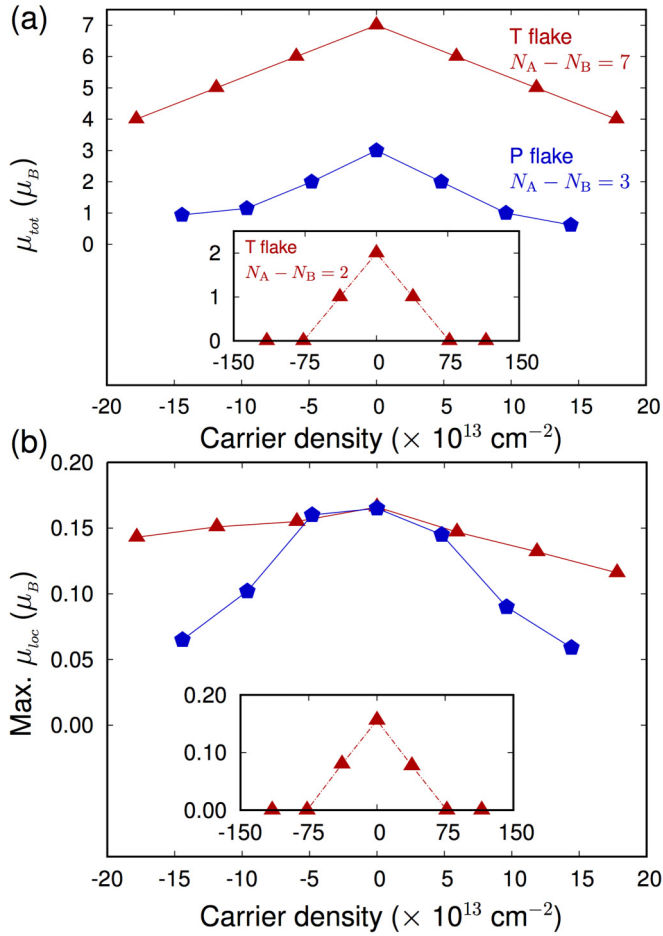


FIG. 4. Effect of carrier (electron and hole) doping on the magnetism for $N_A \neq N_B$ flakes. Calculated (a) total moment μ_{tot} and (b) maximum local moment on the edge μ_{loc} with varied carrier doping for T flakes with $m = 3$ and 8 and a $4 \otimes 7$ P flake. Positive (negative) doping indicates electron (hole) doping.

populates the minority p_z channel of the B sublattice, as seen in Fig. 5(d). Thus, the decrease in μ_{tot} becomes slower than expected [Fig. 4(a)]. Interestingly, for all $N_A \neq N_B$ flakes, although the calculated μ_{loc} and μ_{tot} decrease upon carrier doping, the intrinsic intraedge and interedge magnetic couplings remain the same as for the undoped flakes.

In contrast, carrier doping affects the magnetism in $N_A = N_B$ flakes in a nontrivial fashion. As discussed earlier, a nonmagnetic to compensated ferrimagnetic phase change occurs at a critical size characterized by $\delta_{AB} < 0.07$ [Fig. 2(a)]. Here, we consider R and H flakes with $\delta_{AB} < 0.07$, which are magnetic in their neutral state, and investigate the effect of carrier doping. Interestingly, we find a magnetic phase change beyond a critical carrier density [Figs. 6(a) and 6(b)]. The interedge coupling becomes ferromagnetic with nonzero μ_{tot} [Figs. 6(c) and 6(d)]. It would be interesting to investigate the variation of μ_{loc} with doping, especially around the critical density at which the magnetic phase change occurs. The overall variation of μ_{loc} in these flakes is found to be qualitatively similar to those for the T and P flakes [Fig. 4(b)]. The maximum values of μ_{loc} for the neutral 7×7 R flake and $m = 10$ H flakes are found to be $0.16 \mu_B$ and $0.14 \mu_B$, respectively.

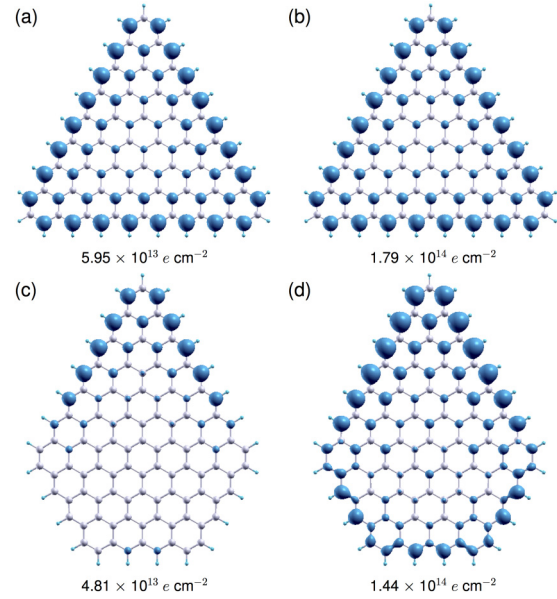


FIG. 5. The partial charge-density distribution for the doped electron, calculated for an $m = 8$ T flake ($N_A - N_B = 7$) and a $4 \otimes 7$ P flake ($N_A - N_B = 3$). For the T flake, the doped electron is distributed mainly over the edge and only on a particular sublattice, independent of doped carrier density, as is evident from a comparison of (a) and (b). In contrast, for the P flake, the distribution of the doped carrier depends on the carrier density. While at a lower density it is distributed over the edge and only on a particular sublattice as in the case of the T flake [see (c)], the doped carrier is distributed over both the sublattices at higher concentration [shown in (d)]. The overall picture for hole doping is found to be similar, which is not shown.

Around the critical doping density, which is 4.05×10^{13} for both electron doping and hole doping in the case of R flakes, the maximum μ_{loc} is calculated to be $0.14 \mu_B$ and $0.13 \mu_B$ for electron doping and hole doping, respectively. In comparison, the maximum μ_{loc} in H flakes is found to be $0.09 \mu_B$ and $0.12 \mu_B$ for critical electron doping and hole doping of 1.56×10^{13} and 2.33×10^{13} , respectively. Thus, although the local moments show some variation upon doping, the systems remain magnetic, unlike in the case of $N_A \neq N_B$ flakes.

The overall impact of carrier doping is therefore qualitatively different in these flakes compared to the flakes with a sublattice imbalance. While carrier doping affects μ_{loc} and thus μ_{tot} in $N_A \neq N_B$ flakes without affecting the nature of long-range order, a magnetic phase transition is observed for $N_A = N_B$ flakes. Further, the electron-hole asymmetry is observed in terms of stabilization of a particular magnetic phase [Figs. 6(a) and 6(b)], although the phase transition is induced by both electron doping and hole doping. In the case of R flakes, we notice a possible reentrance to the compensated ferrimagnetic phase as the energy difference $E_{\text{AFM}} - E_{\text{FM}}$ decreases at large ρ_c .

C. Effects of carried doping on electronic structure

Although bulk graphene is a semimetal with zero density of states at the Dirac points, the electronic structure of graphene quantum dots and ribbons depends sensitively on the

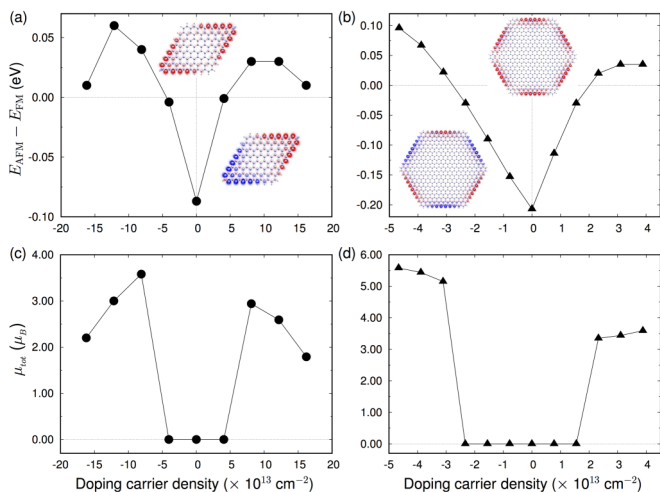


FIG. 6. Effect of carrier doping on magnetic $N_A = N_B$ flakes. Calculated energy differences between the compensated ferrimagnetic (AFM) and ferromagnetic (FM) solutions for (a) a 7×7 R flake and (b) an $m = 10$ H flake. The insets show representative magnetization densities. The corresponding total moments μ_{tot} are shown in (c) and (d).

crystallographic orientation of their edges [11,25,26,48–52]. Although conventional DFT is known to underestimate the band gap, here, we are mainly interested in the qualitative dependence of band gaps with flake size. The neutral flakes, considered in the present study, are found to be semiconducting regardless of their shape and size, and the calculated gaps are found to decrease with increasing flake size, characterized by the total number of atoms N in the flake (Fig. 7). Although the gap should go to zero at infinite size, the asymptotic interpolation might be complex [51,52] due to the intricate dependence on the flake shape and corresponding magnetism. Given the semiconducting nature of neutral flakes under study, it would be worthwhile to investigate the effect of carrier doping. We observe an electronic phase transition in these

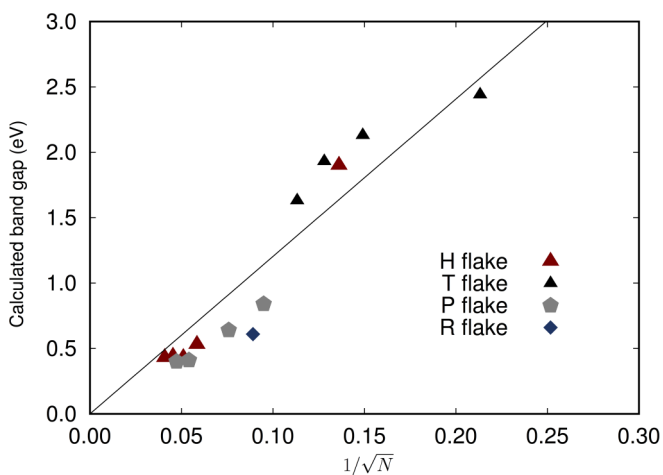


FIG. 7. Calculated band gap for the flakes with different shapes and sizes, where N is the number of carbon atoms in the respective nanoflake. The solid line is a linear fit indicating that the band gap decreases with increasing flake size.

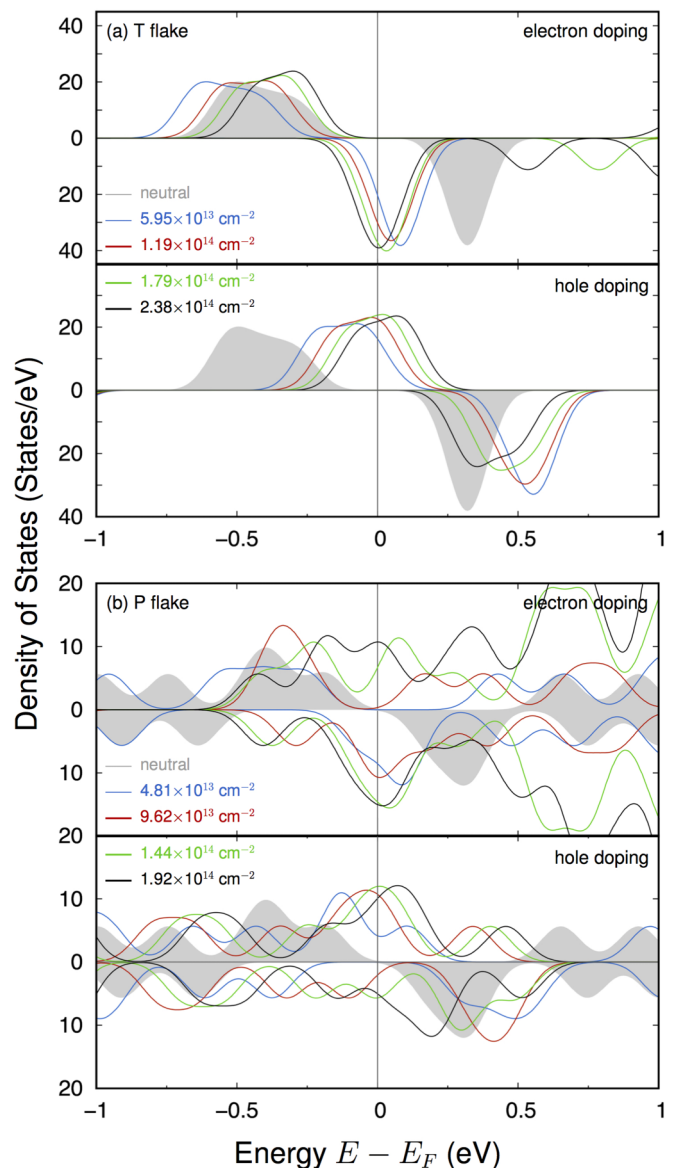


FIG. 8. Evolution of the electronic structure with carrier doping for (a) an $m = 8$ T flake and (b) a 4×7 P flake. While a semiconductor–half-metal transition is observed for the T flake, a semiconductor–half-metal–metal transition is observed for the P flake.

flakes. In particular, a semiconductor to (half) metal transition is observed due to carrier doping.

We first investigate the $N_A \neq N_B$ flakes in detail, for which we particularly consider the $m = 8$ T and 4×7 P flakes. The neutral $m = 8$ T flake is a semiconductor with a 1.29 (1.27) eV gap in the majority (minority) channel. Single-electron (-hole) doping with corresponding $\rho_c = 5.95 \times 10^{13} \text{ cm}^{-2}$ alters the electronic structure and transforms the flake into half metallic [Fig. 8(a)]. The flake remains half metallic upon further doping. The otherwise unoccupied minority p_z channel gets populated by electron doping [Fig. 8(a)], and thus, the minority channel becomes conducting. In contrast, for hole doping, electrons are removed from the majority p_z channel, and thus, the Fermi level E_F moves lower in energy. This shifting of

the Fermi Level upon carrier doping leads to a gap closing in the majority (minority) channel under hole (electron) doping [Fig. 8(a)]. The solution remains half metallic [Fig. 8(a)] at all carrier doping studied in the present work. Thus, the T flake is expected to manifest completely spin polarized transport under applied gate voltage. Further, it would be possible to control conduction in a particular channel (majority or minority) by controlling the polarity of the gate voltage (electron or hole doping). This control would have significant importance in the context of spin-based electronics.

The carrier-induced evolution of electronic structure in P flakes is qualitatively different. A semiconductor to half-metal to metal transition is observed with increasing carrier density. The neutral 4×7 P flake is semiconducting with a 0.55 (0.51) eV gap in the majority (minority) channel. For electron

doping with $\rho_c \leq 9.62 \times 10^{13} \text{ cm}^{-2}$, the doped electron populates only the minority channel, and the flake becomes half metallic [Fig. 8(b)]. A further increase in electron density populates both majority and minority channels simultaneously, and a metallic solution emerges for $\rho_c \geq 1.44 \times 10^{14} \text{ cm}^{-2}$. In contrast, for hole doping, electrons are removed only from the majority channel for $\rho_c \leq 9.62 \times 10^{13} \text{ cm}^{-2}$. As E_F moves lower in energy, a half-metallic solution emerges. A further increase in hole doping depletes electrons from both the channels, and the ground state becomes metallic. This picture also explains the emergence of noninteger μ_{tot} for the corresponding ground state [Fig. 4(a)] and the slow decrease in μ_{tot} for the metallic P flakes at high carrier doping.

We next discuss the carrier-dependent electronic structure for the flakes without sublattice imbalance, $N_A = N_B$. Here, we consider the 7×7 R flake and the $m = 10$ H flake, which show a fully compensated ferrimagnetic structure under the undoped condition. These flakes have 240 and 200 meV semiconducting gaps, respectively, in their neutral states. A semiconductor to metal transition is observed [Figs. 9(a) and 9(b)] for both R and H flakes, without any appearance of a half-metallic solution. As the interedge coupling is antiferromagnetic in the neutral flakes, the doped electron populates both the majority and minority channels. Thus, gaps in both channels disappear, and the flakes become metallic. Similarly, the electrons are depleted from both channels due to hole doping. Thus, E_F continuously shifts to a lower energy, and the solutions become metallic. A similar semiconductor to metal transition has been experimentally observed in graphene nanoribbons [27].

IV. SUMMARY

Using first-principles calculations, we performed a systematic study of the magnetic and electronic structures of graphene nanoflakes with different shapes and sizes. Further, the effect of carrier doping was investigated, which can be accessed experimentally by applying gate voltage. The presence or absence of sublattice imbalance plays a crucial role in magnetism. For flakes without any sublattice imbalance, a nonmagnetic to magnetic phase transition was observed with increasing flake size, which is characterized by the armchair defect concentration δ_{AB} along the edge. We found that beyond a critical flake size $\delta_{AB} < 0.07$, the carbon atoms at the edge develop local moments and the flake becomes magnetic. In contrast, the flakes with sublattice imbalance were always found to be magnetic. Further, for the neutral flakes with any shape, the edge moments from the same sublattice coupled ferromagnetically, while antiferromagnetic coupling was observed between the moments from a different sublattice. This is in agreement with the mean-field solution of the Hubbard model, and in all cases the ground-state magnetization followed Lieb's prediction, $\mu_{\text{tot}} = (N_A - N_B)$.

We found that the magnetic phase transition is induced by carrier doping. For $N_A = N_B$ flakes, beyond a critical doping an antiferromagnetic to ferromagnetic phase transition was observed. In contrast, carrier doping suppresses the magnetism in $N_A \neq N_B$ flakes. In these flakes, the local moments at the

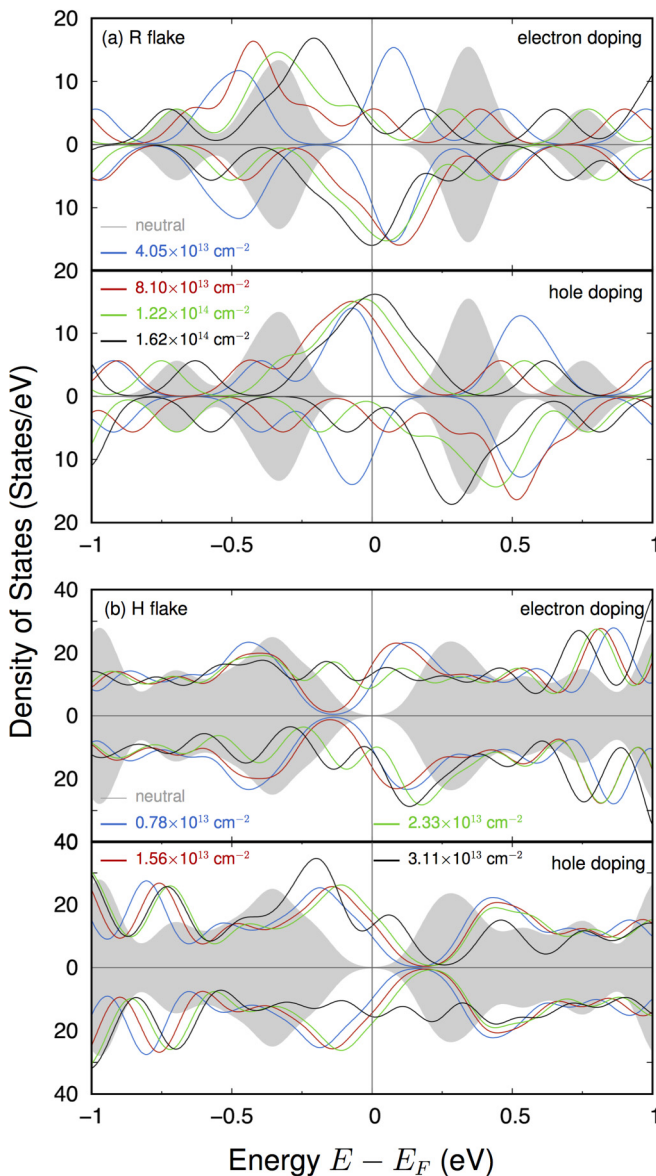


FIG. 9. Carrier-induced electronic structure evolution for (a) a 7×7 R flake and (b) an $m = 10$ H flake. For both flakes a semiconductor-metal transition is observed due to electron/hole doping.

edge and thus μ_{tot} monotonically decrease with increasing doping. This indicates that at very high doping density the flakes may become nonmagnetic. Further, a simultaneous electronic phase transition was observed in response to carrier doping. In this regard, the cases with sublattice imbalance were found to be more interesting. A semiconductor to half-metal transition and a semiconductor to half-metal to metal transition were observed in T and P flakes, respectively. In particular, the half-metallic solution is interesting and may lead to fully polarized transport. In contrast, for the $N_A = N_B$ flakes, a semiconductor to metal transition takes place without an appearance of half-metallic solution. Such concurrent magnetic and electronic phase transitions have been experimentally observed in zigzag graphene nanoribbons [27]. Finally, we propose that a nanolithographic technique coupled with scanning tunneling microscopy will be able to verify our theoretical prediction of complex size- and

shape-dependent magnetic and electronic phase transitions in graphene flakes, which may lead to electronic and spintronics applications.

ACKNOWLEDGMENTS

Some of the reported calculations were done using the supercomputing facilities at the Centre for Development of Advanced Computing, Pune; Inter University Accelerator Centre, Delhi; and the Center for Computational Materials Science, Institute of Materials Research, Tohoku University. S.G. and T.S.-D. acknowledge the computation facility provided by the Thematic Unit of Excellence on Computational Materials Science. M.K. acknowledges the funding from the Department of Science and Technology, government of India, under a Ramanujan Fellowship and Nano Mission project SR/NM/TP-13/2016(G).

-
- [1] A. Rycerz, J. Tworzydło, and C. W. J. Beenakker, *Nat. Phys.* **3**, 172 (2007).
- [2] O. V. Yazyev, *Rep. Prog. Phys.* **73**, 056501 (2010).
- [3] S. Roche and S. O. Valenzuela, *J. Phys. D* **47**, 094011 (2014).
- [4] W. Han, R. K. Kawakami, M. Gmitra, and J. Fabian, *Nat. Nanotechnol.* **9**, 794 (2014).
- [5] Z. Bullard, E. C. Girão, J. R. Owens, W. A. Shelton, and V. Meunier, *Sci. Rep.* **5**, 7634 (2015).
- [6] B. Trauzettel, D. V. Bulaev, D. Loss, and G. Burkard, *Nat. Phys.* **3**, 192 (2007).
- [7] O. V. Yazyev, *Nano Lett.* **8**, 1011 (2008).
- [8] J. Fischer, B. Trauzettel, and D. Loss, *Phys. Rev. B* **80**, 155401 (2009).
- [9] D. M. Edwards and M. I. Katsnelson, *J. Phys. Condens. Matter* **18**, 7209 (2006).
- [10] O. V. Yazyev and M. I. Katsnelson, *Phys. Rev. Lett.* **100**, 047209 (2008).
- [11] Y.-W. Son, M. L. Cohen, and S. G. Louie, *Nature (London)* **444**, 347 (2006).
- [12] O. V. Yazyev and L. Helm, *Phys. Rev. B* **75**, 125408 (2007).
- [13] J. J. Palacios, J. Fernández-Rossier, and L. Brey, *Phys. Rev. B* **77**, 195428 (2008).
- [14] S. S. Alexandre, A. D. Lucio, A. H. C. Neto, and R. W. Nunes, *Nano Lett.* **12**, 5097 (2012).
- [15] R. R. Nair, I. L. Tsai, M. Sepioni, O. Lehtinen, J. Keinonen, A. V. Krasheninnikov, A. H. Castro Neto, M. I. Katsnelson, A. K. Geim, and I. V. Grigorieva, *Nat. Commun.* **4**, 2010 (2013).
- [16] Y. Zhang, S.-Y. Li, H. Huang, W.-T. Li, J.-B. Qiao, W.-X. Wang, L.-J. Yin, K.-K. Bai, W. Duan, and L. He, *Phys. Rev. Lett.* **117**, 166801 (2016).
- [17] F. Donati, Q. Dubout, G. Autès, F. Patthey, F. Calleja, P. Gambardella, O. V. Yazyev, and H. Brune, *Phys. Rev. Lett.* **111**, 236801 (2013).
- [18] H. González-Herrero, J. M. Gómez-Rodríguez, P. Mallet, M. Moaied, J. J. Palacios, C. Salgado, M. M. Ugeda, J.-Y. Veuillen, F. Yndurain, and I. Brihuega, *Science* **352**, 437 (2016).
- [19] K. Nakada, M. Fujita, G. Dresselhaus, and M. S. Dresselhaus, *Phys. Rev. B* **54**, 17954 (1996).
- [20] M. Fujita, K. Wakabayashi, K. Nakada, and K. Kusakabe, *J. Phys. Soc. Jpn.* **65**, 1920 (1996).
- [21] Z. Klusek, Z. Waqar, E. Denisov, T. Kompaniets, I. Makarenko, A. Titkov, and A. Bhatti, *Appl. Surf. Sci.* **161**, 508 (2000).
- [22] Y. Kobayashi, K.-i. Fukui, T. Enoki, K. Kusakabe, and Y. Kaburagi, *Phys. Rev. B* **71**, 193406 (2005).
- [23] Y. Kobayashi, K.-i. Fukui, T. Enoki, and K. Kusakabe, *Phys. Rev. B* **73**, 125415 (2006).
- [24] N. Tombros, C. Jozsa, M. Popinciuc, H. T. Jonkman, and B. J. van Wees, *Nature (London)* **448**, 571 (2007).
- [25] M. Y. Han, B. Özyilmaz, Y. Zhang, and P. Kim, *Phys. Rev. Lett.* **98**, 206805 (2007).
- [26] L. A. Ponomarenko, F. Schedin, M. I. Katsnelson, R. Yang, E. W. Hill, K. S. Novoselov, and A. K. Geim, *Science* **320**, 356 (2008).
- [27] G. Z. Magda, X. Jin, I. Hagymasi, P. Vancso, Z. Osvath, P. Nemes-Incze, C. Hwang, L. P. Biro, and L. Tapasztó, *Nature (London)* **514**, 608 (2014).
- [28] J. Fernández-Rossier and J. J. Palacios, *Phys. Rev. Lett.* **99**, 177204 (2007).
- [29] E. H. Lieb, *Phys. Rev. Lett.* **62**, 1201 (1989).
- [30] M. Kabir and T. Saha-Dasgupta, *Phys. Rev. B* **90**, 035403 (2014).
- [31] Y. Nagaoka, *Phys. Rev.* **147**, 392 (1966).
- [32] G. Kresse and J. Hafner, *Phys. Rev. B* **47**, 558 (1993).
- [33] G. Kresse and J. Furthmüller, *Phys. Rev. B* **54**, 11169 (1996).
- [34] P. E. Blöchl, *Phys. Rev. B* **50**, 17953 (1994).
- [35] J. P. Perdew, K. Burke, and M. Ernzerhof, *Phys. Rev. Lett.* **77**, 3865 (1996).
- [36] S. L. Dudarev, G. A. Botton, S. Y. Savrasov, C. J. Humphreys, and A. P. Sutton, *Phys. Rev. B* **57**, 1505 (1998).
- [37] G. Makov and M. C. Payne, *Phys. Rev. B* **51**, 4014 (1995).
- [38] J. Lento, J.-L. Mozos, and R. M. Nieminen, *J. Phys. Condens. Matter* **14**, 2637 (2002).
- [39] I. Dabo, B. Kozinsky, N. E. Singh-Miller, and N. Marzari, *Phys. Rev. B* **77**, 115139 (2008).
- [40] S. E. Taylor and F. Bruneval, *Phys. Rev. B* **84**, 075155 (2011).

- [41] B. Huang, F. Liu, J. Wu, B.-L. Gu, and W. Duan, *Phys. Rev. B* **77**, 153411 (2008).
- [42] T. O. Wehling, E. Şaşıoğlu, C. Friedrich, A. I. Lichtenstein, M. I. Katsnelson, and S. Blügel, *Phys. Rev. Lett.* **106**, 236805 (2011).
- [43] Z. Y. Meng, T. C. Lang, S. Wessel, F. F. Assaad, and A. Muramatsu, *Nature (London)* **464**, 847 (2010).
- [44] S. Sorella and E. Tosatti, *Europhys. Lett.* **19**, 699 (1992).
- [45] T. Paiva, R. T. Scalettar, W. Zheng, R. R. P. Singh, and J. Oitmaa, *Phys. Rev. B* **72**, 085123 (2005).
- [46] V. E. Dorgan, M.-H. Bae, and E. Pop, *Appl. Phys. Lett.* **97**, 082112 (2010).
- [47] J. Ye, M. F. Craciun, M. Koshino, S. Russo, S. Inoue, H. Yuan, H. Shimotani, A. F. Morpurgo, and Y. Iwasa, *Proc. Natl. Acad. Sci. USA* **108**, 13002 (2011).
- [48] V. Barone, O. Hod, and G. E. Scuseria, *Nano Lett.* **6**, 2748 (2006).
- [49] Y.-W. Son, M. L. Cohen, and S. G. Louie, *Phys. Rev. Lett.* **97**, 216803 (2006).
- [50] X. Li, X. Wang, L. Zhang, S. Lee, and H. Dai, *Science* **319**, 1229 (2008).
- [51] S. K. Singh, M. Neek-Amal, and F. M. Peeters, *J. Chem. Phys.* **140**, 074304 (2014).
- [52] W. Hu, L. Lin, C. Yang, and J. Yang, *J. Chem. Phys.* **141**, 214704 (2014).